supplementary information

Iron-doped bimetallic borides Fe-Ni_2B-*x* nanoparticle toward efficient oxygen evolution reaction at a large current density

Yajuan Zhang[a,b], Hui Xu[a*], Xingwei Shi[b*], Shengyue Ma[a,b]

[a] *College of Petrochemical Technology, Lanzhou University of Technology, Lanzhou, 730050, China.*

[b] *Ionic Liquids and Low Carbon Energy Research Division, Institute of Process Engineering, Chinese Academy of Sciences, Beijing, 100190, china.*

[*] Corresponding author.

E-mail: xuhui@lut.edu.cn (H. Xu); xwshi@ipe.ac.cn (X. Shi).

Experimental

Materials and reagents

Trisodium citrate dihydrate ($C_6H_5Na_3O_7$, AR) and nickel sulfate ($NiSO_4·6H_2O$, AR) were bought from Aladdin (Shanghai, China). Dimethyl ammonium borane (Et_2NHBH_3, DMAB, AR), ammonium fluoride (NH_4F, AR), Iridium oxide (IrO_2) and Nafion (5 wt%) were purchased from Macklin. Ammonium iron(II) sulfate ($Fe(NH_4)_2·(SO_4)_2·6H_2O$, AR), acetone (AR, 99.5%), ethanol (AR, 99.5%), hydrochloric acid (HCl, AR) and potassium hydroxide (KOH, AR) was purchased from Sinopharm Chemical Reagent Company. Nickel foam (NF) about 0.1 mm in thickness were purchased from Shanghai Metal Company. All chemicals were used as received without further purification. NF (about 1×2 cm) was ultrasonic treated with 1M HCl solution, acetone, ethanol for 30 min, respectively, removing the organic impurity and NiO layer on the surface of NF, finally vacuum drying at 60 °C for 24h.

Synthesis of catalysts Fe-Ni_2B/NF-*x* (*x*=1, 2, 3, 4)

Taking the preparation of Fe-Ni_2B/NF-3 as an example. Firstly, treated NF was immersed in a 100 mL mixture solution that consist of trisodium citrate dehydrate ($C_6H_5Na_3O_7$, 2 g), ammonium fluoride (NH_4F, 1.5 g), nickel sulfate ($NiSO_4·7H_2O$, 2.5 g) and borane dimethylamine complex (DMAB, 0.72 g). The Ni_2B nanoparticles was uniformly grown on NF with reaction 60 min under 40℃ water bath condition. Then, the Ni_2B/NF precursor was transferred into 0.3 mmol ammonium iron(II) sulfate ($Fe(NH_4)_2(SO_4)_2·6H_2O$) solution with keeping for 12h at the room temperature and vacuum drying at 60℃. Subsequently, the sample was placed on the porcelain

boat and center of a quartz tube, respectively. Before high-temperature pyrolysis, Ar was purged for 10 min to remove the air. The Fe-Ni_2B/NF-*x* was heated at 300℃ with a rate of 2℃ min^{-1} and maintained at 300℃ for 1h. The iron-doped bimetallic borides Fe-Ni_2B/NF-*x* catalyst was obtained with loading approximately 3.6 mg cm^{-2}. Annealing treatment promoted the crystal structure transformation of precursor Ni_2B/NF (details seeing Figure S3), which exhibits the excellent electrochemical properties when annealed temperature is 300 °C (activated-Ni_2B/NF, the Ni_2B/NF mentioned in the text have been annealed unless otherwise noted). In addition, Fe-Ni_2B/NF-1, Fe-Ni_2B/NF-2, Fe-Ni_2B/NF-4 electrodes are prepared with the same way as Fe-Ni_2B/NF-3 except for the amount of $Fe(NH_4)_2(SO_4)_2 \cdot 6H_2O$ is 0.1, 0.2 and 0.4 mmol, respectively.

Characterizations

X-ray diffractometer (XRD) was tested on a Rigaku D/MAX 2550 with Cu Kα radiation. The scanning electron microscope (SEM) measurements were performed on a HitachiS-4800 field at an accelerating voltage of 20 kV. Transmission electron microscopy (TEM) was done on an JEOL JEM-F200 transmission electron microscope at an acceleration voltage of 200 kV. Raman spectra were collected on a Renishaw in Via microscope with an excitation laser of 532 nm. X-ray photoelectron spectrometer (XPS) data were collected on an Thermo Scientific K-Alpha using Al Kα ray as the exciting source. Fourier transform infrared (FT-IR) spectra were recorded on a Thermo-Nicolet-380 spectrometer.

Electrochemical measurements

The as-prepared electrodes were measured with a Versa STAT 3F electrochemical workstation in a three-electrode cell system using 1.0 M KOH electrolyte. The as-prepared catalysts Fe-Ni_2B/NF-*x* as working electrode, a graphite rod as the counter electrode, Hg/HgO as the reference electrode, respectively. All potentials measured were calibrated to the reversible hydrogen electrode (RHE) via Nernst equation. The polarization curves were conducted using LSV at a scan rate of 5 mV s^{-1}. Moreover, LSV curves were corrected with *iR*-compensation (80%) based on the values of solution resistance (R_s) by testing EIS spectra. Electrochemical impedance spectroscopy (EIS) was measured within a frequency range of 0.01 Hz to 0.1 MHz in the 1.0 M KOH solution was tested. The double-layer capacitance (Cdl) was recorded by deriving from the cyclic voltammery (CV) curves versus the scan rates. The electrochemical active surface areas (ECSA) were determined from the capacitance measurements in the potential region of no faradic reaction occur at different scan rates. The long-term durability measurements were conducted through using the CV and chronopotentiometry response at a constant current density for a certain time.

Density functional theory computational details

All structure relaxations and electronic properties calculations within spin-polarized density-functional theory (DFT) were executed in Vienna ab initio Simulation Package (VASP). The exchange correlation interactions of electrons were described by Perdew Burke Ernzerhof (PBE) functional within generalized gradient

approximation (GGA). A cut-off energy of 500eV was adopted to Perdew Burke Ernzerhof (PBE) exchange correlation functional, the DFT-D3 methods was performed to consider the van der Waals (vdW) interactions. In order to avoid the interlayer interaction was introduced by the periodic boundary condition, a sufficient vacuum was inserted to 20Å in the z direction. The Brillouin zone was sampled by 5×5×1 Monkhorst-Pack (MP) grid for structural relaxation. The convergence criteria for energy and force were set to be 10-6 eV and 0.02 eV/Å, respectively. According to the computational hydrogen electrode (CHE) model which was proposed by Nørskov et al; the formation energy of OER intermediate species was performed by using the concept of the electron-proton pair ($H^+ + e^-$), the energies of gas molecules (such as H_2O, H_2, and O_2) were taken from NIST database.

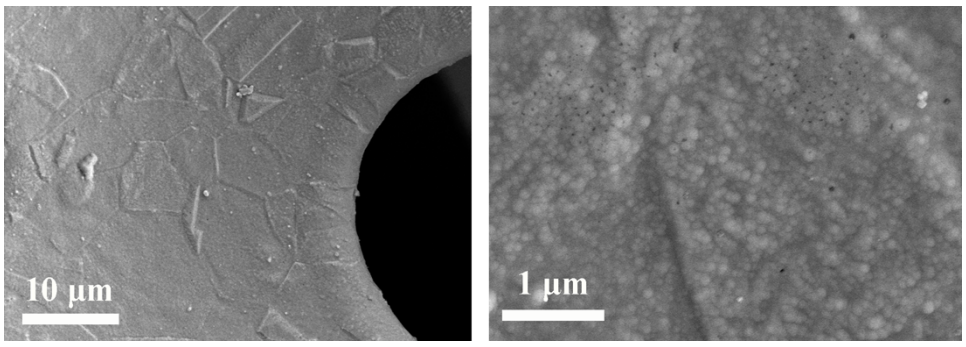

Figure S1 The SEM images of the precursor Ni_2B/NF.

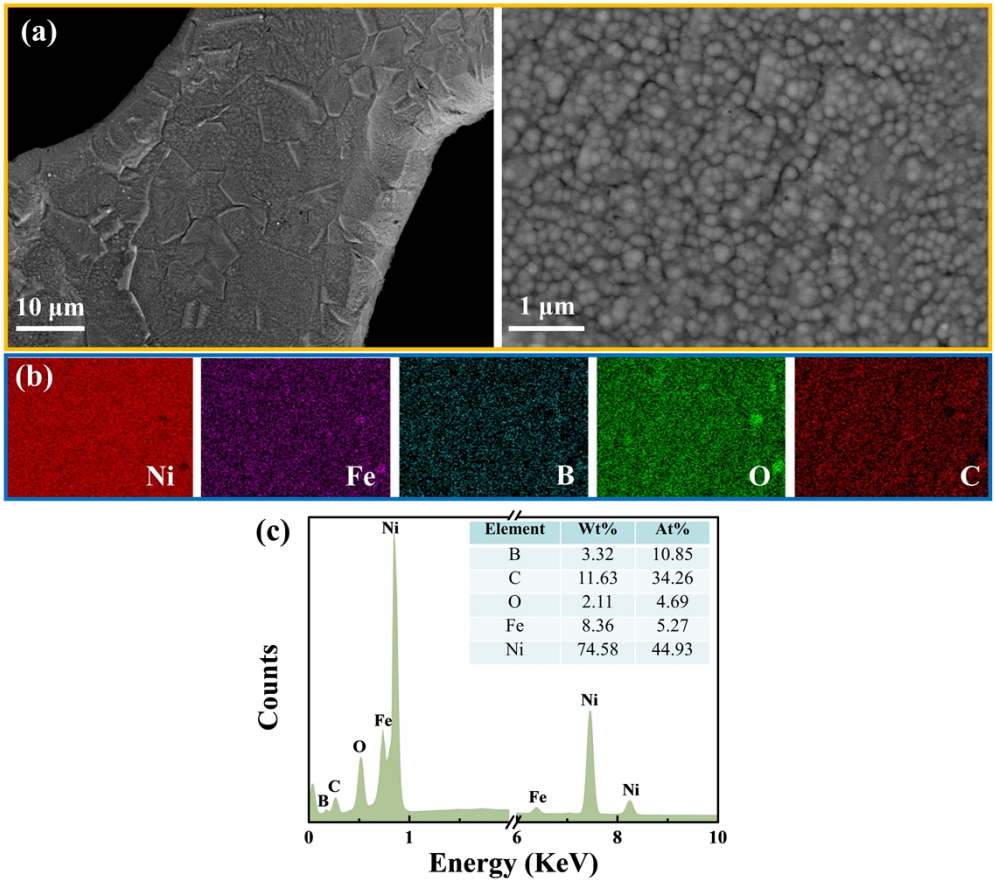

Figure S2 The (a) SEM images, (b) EDS elemental mapping images and (c) EDS spectrum of the catalyst electrode Fe-Ni_2B/NF-3.

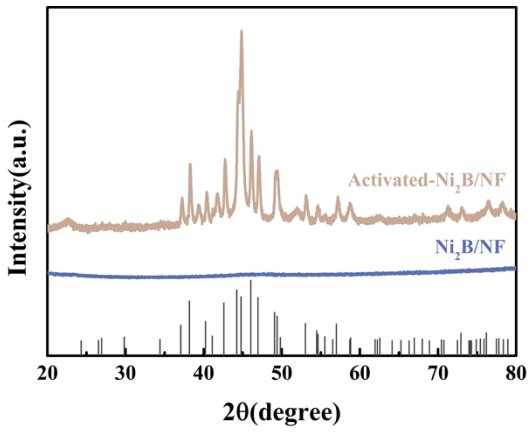

Figure S3 The Effect of annealing temperature on crystal structure of the electrode Ni_2B/NF.

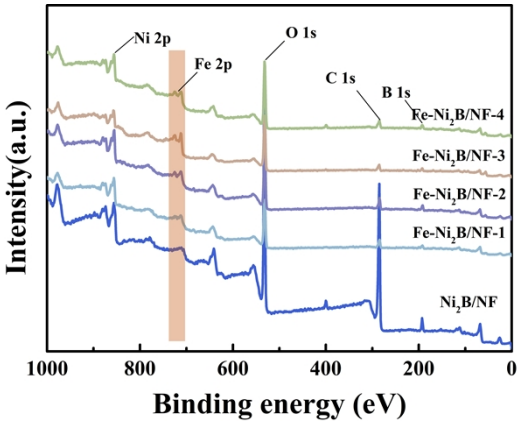

Figure S4 The full spectrum of Fe-Ni_2B/NF-x (x=1, 2, 3, 4).

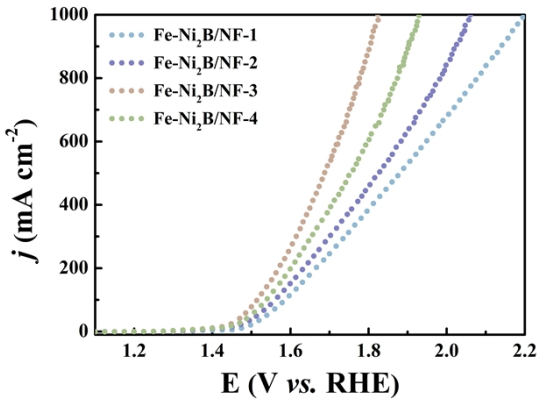

Figure S5 Without *iR*-compensation polarization curves of Fe-Ni_2B/NF-*x* (x=1, 2, 3, 4) in 1 M KOH.

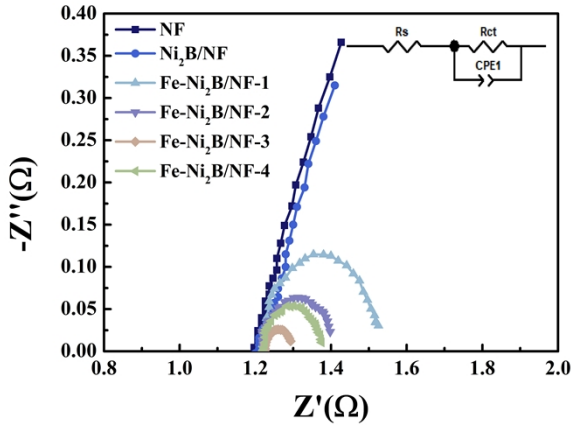

Figure S6 Nyquist plots of the electrode NF, Ni_2B/NF and Fe-Ni_2B/NF-*x* (*x*=1, 2, 3, 4) in 1 M KOH.

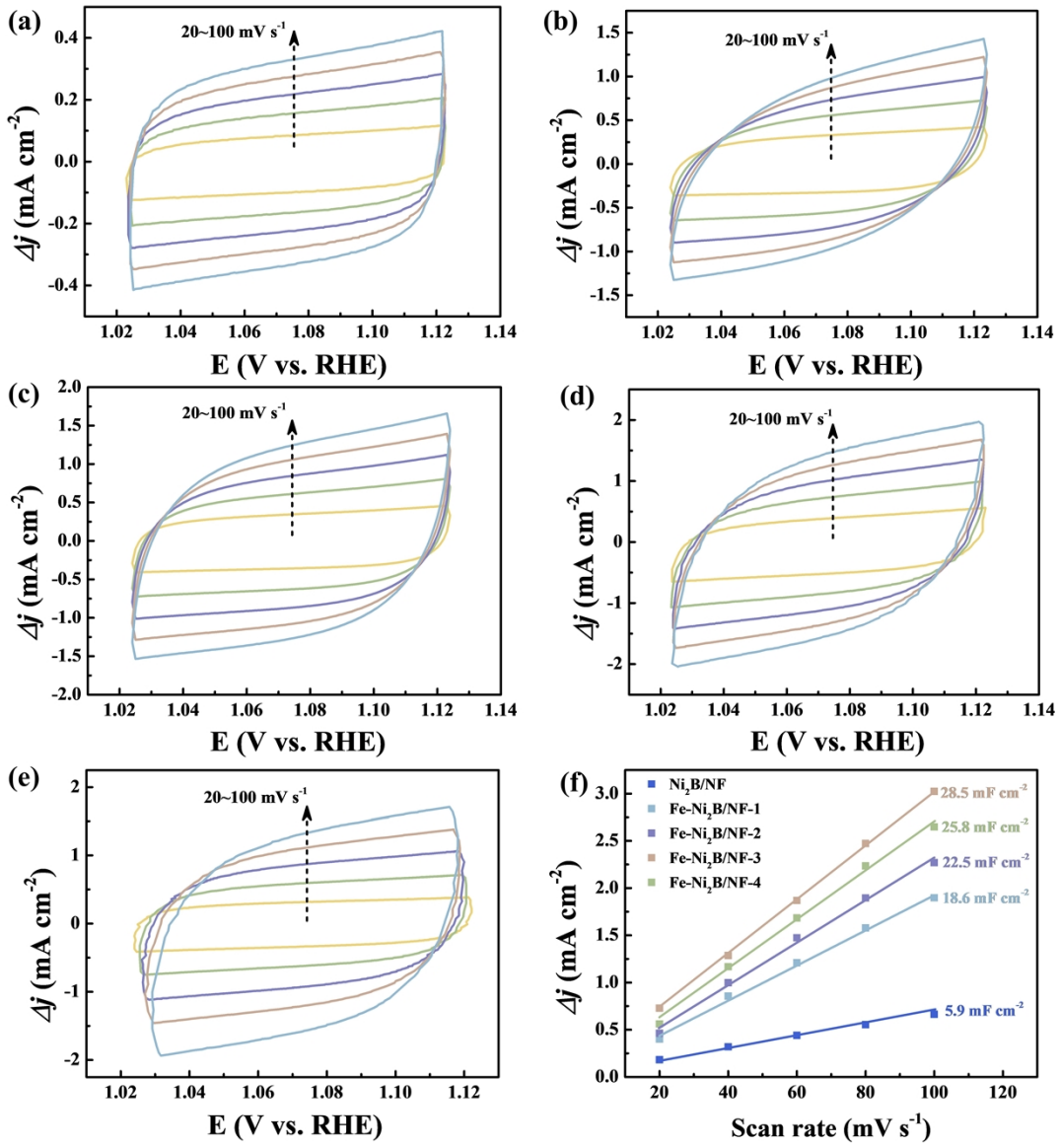

Figure S7 (a-b) CV curves of Ni_2B/NF and Ni_2B/NF-x (x=1, 2, 3, 4) at different scanning rates. (c) Double-layer capacitive currents of electrode of Fe-Ni_2B/NF- x (x=1, 2, 3, 4) and Ni_2B/NF.

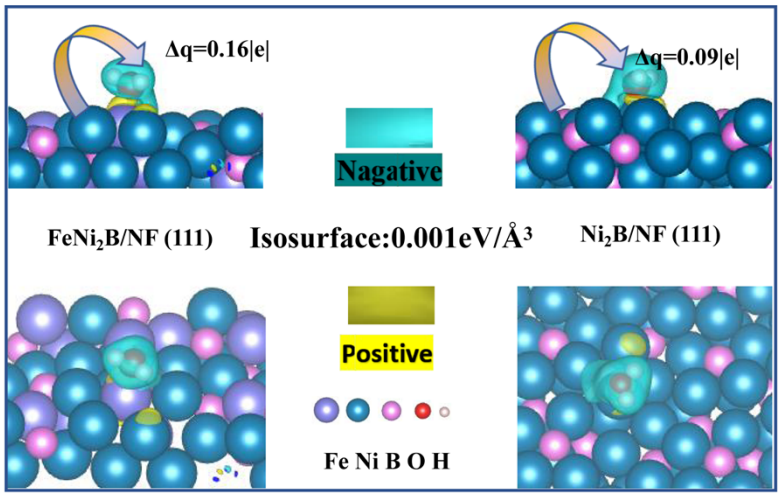

Figure S8 The calculated charge density differences of (a) $FeNi_2B$/NF (111) and (b) Ni_2B/NF (111).

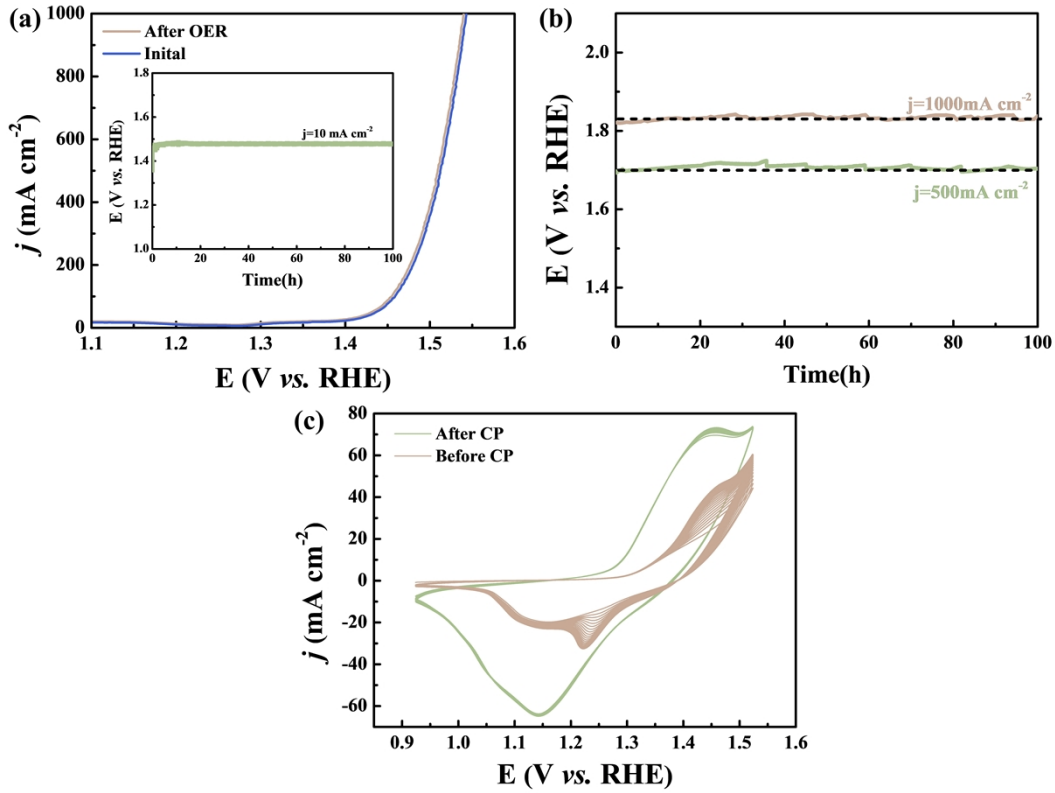

Figure S9 (a) The 5000 CV cycles of Fe-Ni_2B/NF-3 with the range from 0.92 to 2.12 *vs*. RHE and chronopotentiometry with insert a small figure. (b) Chronopotentiometry curves at the current density of 500 and 1000 mA cm^{-2}. (c) The CVs of Fe-Ni_2B/NF-3 by continuous potential between 0.92 and 1.55 V at 100 mV s^{-1} in 1.0 m KOH.

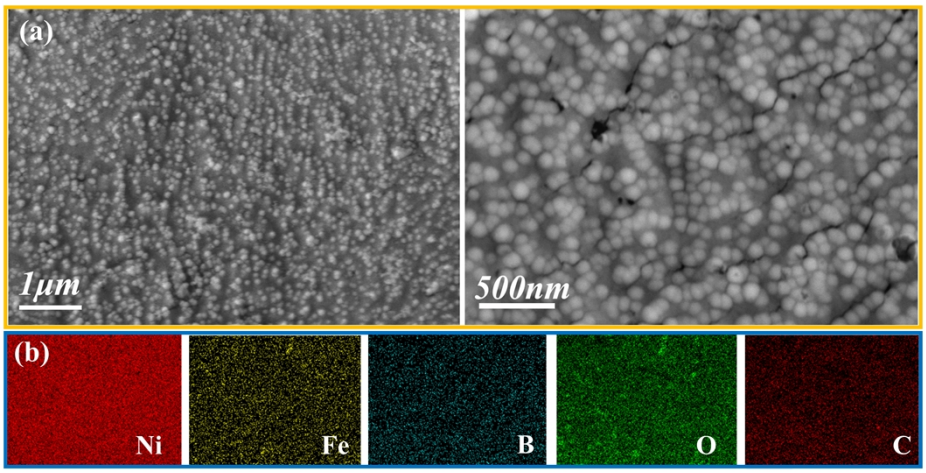

Figure S10 (a) SEM images and (b) EDS elemental mapping images of Fe-Ni_2B/NF-3 after 100h stability test.

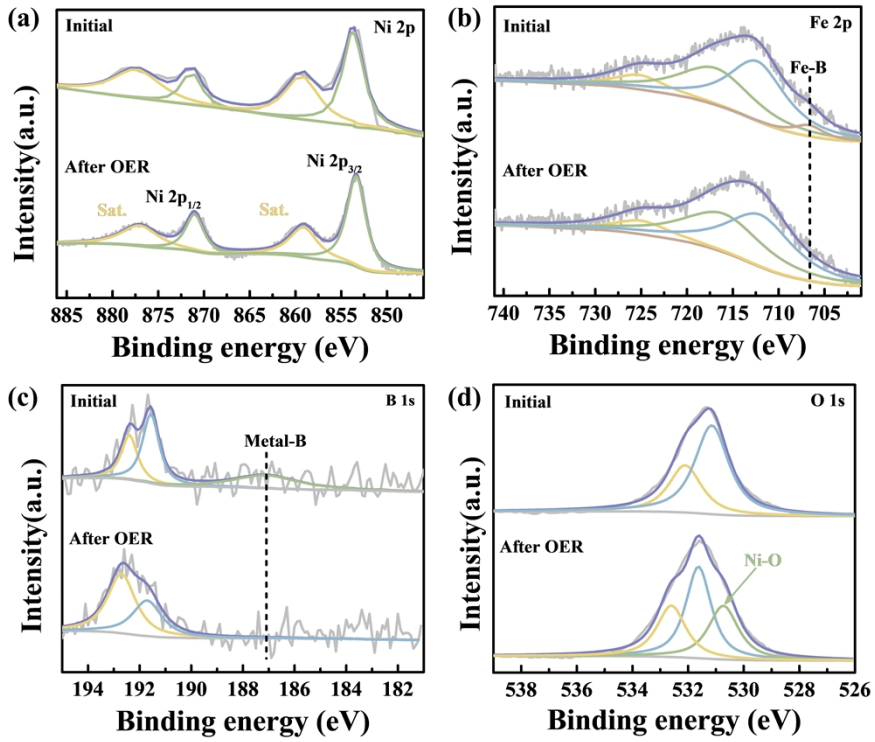

Figure S11 The high-resolution scans of Fe-Ni_2B/NF-3 with the initial and after 100h stability test. (a) Ni 2p, (b) Fe 2p, (c) B 1s and (d) O 1s.

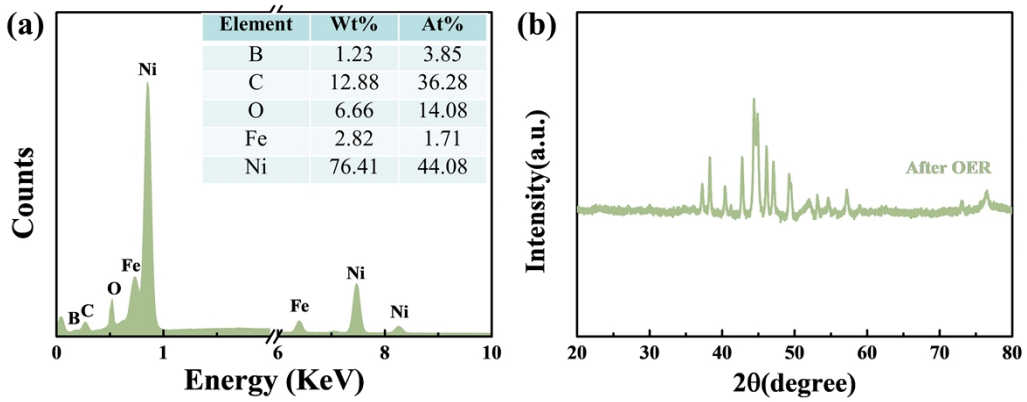

Figure S12 (a) EDS and (b) XRD images of Fe-Ni_2B/NF-3 after 100h stability test.

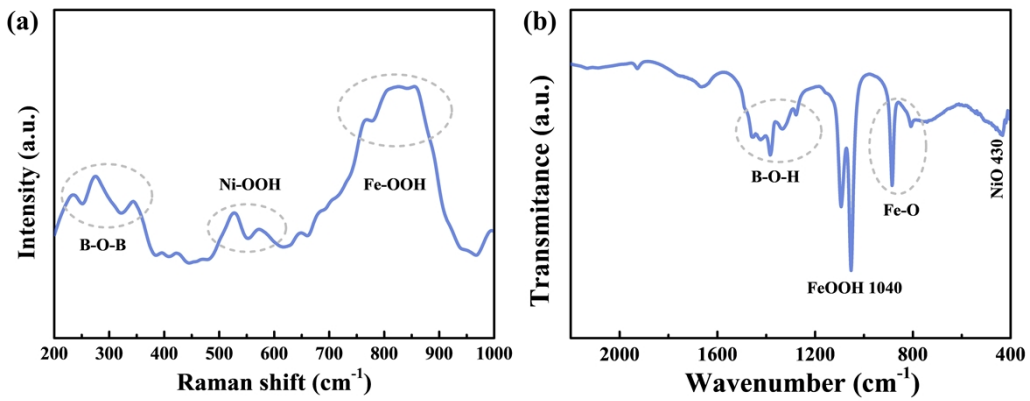

Figure S13 (a) Raman and (b) FTIR spectra of Fe-Ni_2B/NF-3 after OER test. Raman spectroscopy at an excitation wavelength of 532 nm was conducted. The wavenumber around 200～400 cm^{-1} attributed to the vibration peak of B-O-B. The two observed peaks at 530 and 577 cm^{-1} match well with $\delta(Ni^{III}\text{-}O)$ and $\nu(Ni^{III}\text{-}O)$ vibrations of NiOOH, respectively. In addition, the shifts was emerged at 658～850 cm^{-1} could be attributed to an FeOOH. This results analysis confirm that the borate atom promote surface metal was oxidized. Meanwhile, in order to further understand the role of borate, the Fourier transform infrared (FTIR) spectrum was measured. The band at 1600～1200 cm^{-1} are ascribed to the B-O-H bending modes in metaborate. The band at 1060 and 1140 cm^{-1} corresponds to the bending vibration of O-H mode in metal-OOH.

Table S1 Atomic ratio for Ni_2B/NF and Fe-Ni_2B/NF-*x* (*x*=1, 2, 3, 4) OER electrocatalyst comes from XPS measurments.

Catalysts	Atomic (%)		Ni/Fe
	Ni	**Fe**	
Ni_2B/NF	16.10	--	--
Fe-Ni_2B/NF-1	12.12	3.32	0.4/1.6
Fe-Ni_2B/NF-2	11.19	3.98	0.6/1.4
Fe-Ni_2B/NF-3	9.06	4.43	0.8/1.2
Fe-Ni_2B/NF-4	7.58	6.61	1/1

Table S2 Comparison of the OER catalytic performance of Fe-Ni_2B/NF-*x* (*x*=1, 2, 3, 4) and other electrocatalyst electrodes in 1.0 M KOH.

Catalysts	*j* (mA cm^{-2})	η (mV)	Reference
Fe-Ni_2B/NF-1	**10**	**260**	**This work**
Fe-Ni_2B/NF-2	**10**	**215**	
Fe-Ni_2B/NF-3	**10**	**194**	
Fe-Ni_2B/NF-4	**10**	**205**	
np-NiMnFeMo	10	265	[1]
$Ni_{SA}Fe_{SA}$-Ni_xFe/CNT	10	227	[2]
NFN-MOF/NF	10	240	[3]
Ni-P-B/Paper	50	263	[4]
Ni-Mo-B/HF	10	230	[5]
NiCo@C-NiCoMoO/NF	10	260	[6]
Co-P-B	10	290	[7]
Co-Mo-B-P/CF	10	275	[8]
$FeCoB_2$	10	295	[9]
Ni_3FeN/r-GO	10	270	[10]
Cr-doped FeNi-/NCN	10	240	[11]
NiCoP/NF	10	253	[12]
FeCoSe@NCNSs	10	320	[13]
CoFe-PBA-B	10	255	[14]
NC-NiCu-NiCuN	10	232	[15]
$CoNi/CoFe_2O_4$/NF	10	230 (±2)	[16]
CeO*x*-NiB@NF	10	274	[17]
Mo_2NiB_2	10	280	[18]
$NiMoP_2$-Ni_2P	10	258	[19]
$Ni_xFe_{1-x}B$	10	282	[20]
np-$(Ni_{0.67}Fe_{0.33})_4P_5$	10	245	[21]

Table S3 EIS calculation parameters of Ni_2B/NF and Fe-Ni_2B/NF-*x* (*x*=1, 2, 3, 4) from equivalent circuit model.

Sample	Rs (Ω)	Rct (Ω)	CPE-T	CPE-P
Ni_2B/NF	1.37	5.96	0.091	0.711
Fe-Ni_2B/NF-1	1.29	0.35	0.034	0.743
Fe-Ni_2B/NF-2	1.24	0.19	0.040	0.743
Fe-Ni_2B/NF-3	1.22	0.07	0.035	0.806
Fe-Ni_2B/NF-4	1.26	0.16	0.037	0.743

Reference

1. H. Liu, C. Xi, J. Xin, G. Zhang, S. Zhang, Z. Zhang, Q. Huang, J. Li, H. Liu and J. Kang, *Chem. Eng. J.*, 2021, **404**, 126530.
2. W. Luo, Y. Wang, L. Luo, S. Gong, M. Wei, Y. Li, X. Gan, Y. Zhao, Z. Zhu and Z. Li, *ACS Catal.*, 2022, **12**, 1167-1179.
3. D. Senthil Raja, X.-F. Chuah and S.-Y. Lu, *Adv. Energy Mate.*, 2018, **8**, 1801065.
4. W. Hao, R. Wu, H. Huang, X. Ou, L. Wang, D. Sun, X. Ma and Y. Guo, *Energy Environ Sci*, 2020, **13**, 102-110.
5. H. Liu, X. Li, L. Chen, X. Zhu, P. Dong, M. O. L. Chee, M. Ye, Y. Guo and J. Shen, *Adv. Funct. Mater.*, 2021, **32**, 2107308.
6. B. Jiang, K. Liang, Z. Yang, K. Guo, F. Shaik and J. Zheng, *Electrochim. Acta*, 2021, **386**, 138459.
7. A. Chunduri, S. Gupta, O. Bapat, A. Bhide, R. Fernandes, M. K. Patel, V. Bambole, A. Miotello and N. Patel, *Appl. Catal. B: Environ.*, 2019, **259**, 118051.
8. Y. Wei, P. Zou, Y. Yue, M. Wang, W. Fu, S. Si, L. Wei, X. Zhao, G. Hu and H. L. Xin, *ACS Appl. Mater. Interfaces.*, 2021, **13**, 20024-20033.
9. X. Zou, W. Zhang, X. Zhou, K. Song, X. Ge and W. Zheng, *J. Energy Chem.*, 2022, **72**, 509-515.
10. Y. Gu, S. Chen, J. Ren, Y. A. Jia, C. Chen, S. Komarneni, D. Yang and X. Yao, *ACS Nano*, 2018, **12**, 245-253.

11. Y. Wu, X. Tao, Y. Qing, H. Xu, F. Yang, S. Luo, C. Tian, M. Liu and X. Lu, *Adv. Mater.*, 2019, **31**, e1900178.

12. H.-S. Hu, Y. Li, Y.-R. Shao, K.-X. Li, G. Deng, C.-B. Wang and Y.-Y. Feng, *J. Power Sources*, 2021, **484**, 229269.

13. Y. Pan, M. Wang, M. Li, G. Sun, Y. Chen, Y. Liu, W. Zhu and B. Wang, *J. Energy Chem.*, 2022, **68**, 699-708.

14. S. Wang, R. Zhao, T. Zheng, Y. Fang, W. Wang and W. Xue, *J. Colloid Interface Sci.*, 2022, **618**, 34-43.

15. J. Hou, Y. Sun, Z. Li, B. Zhang, S. Cao, Y. Wu, Z. Gao and L. Sun, *Adv. Funct. Mater.*, 2018, **28**, 1803278.

16. S. Li, S. Sirisomboonchai, A. Yoshida, X. An, X. Hao, A. Abudula and G. Guan, *J. Mater. Chem. A*, 2018, **6**, 19221-19230.

17. H. Wang, H. Liu, T. Feng, L. Wang, W. Yuan, Q. Huang and Y. Guo, *Dalton. Trans.*, 2022, **51**, 675-684.

18. A. Saad, Y. Gao, K. A. Owusu, W. Liu, Y. Wu, A. Ramiere, H. Guo, P. Tsiakaras and X. Cai, *Small*, 2022, **18**, e2104303.

19. G. Tian, S. Wei, Z. Guo, S. Wu, Z. Chen, F. Xu, Y. Cao, Z. Liu, J. Wang, L. Ding, J. Tu and H. Zeng, *J. Mater. Sci. Technol.*, 2021, **77**, 108-116.

20. W. Hong, S. Sun, Y. Kong, Y. Hu and G. Chen, *J. Mater. Chem. A*, 2020, **8**, 7360-7367.

21. W. Xu, S. Zhu, Y. Liang, Z. Cui, X. Yang and A. Inoue, *J. Mater. Chem. A*, 2018, **6**, 5574-5579.